HHS Public Access

Author manuscript

Nat Methods. Author manuscript; available in PMC 2016 May 18.

Published in final edited form as:

Nat Methods. 2016 January ; 13(1): 67–73. doi:10.1038/nmeth.3656.

Multi-scale photoacoustic tomography using reversibly switchable bacterial phytochrome as a near-infrared photochromic probe

Junjie Yao[1,5], **Andrii A. Kaberniuk**[2,5], **Lei Li**[1,5], **Daria M. Shcherbakova**[2], **Ruiying Zhang**[1], **Lidai Wang**[1,4], **Guo Li**[1], **Vladislav V. Verkhusha**[2,3,6], and **Lihong V. Wang**[1,6]

[1]Department of Biomedical Engineering, Washington University in St. Louis, St. Louis, MO 63130, USA [2]Department of Anatomy and Structural Biology, and Gruss-Lipper Biophotonics Center, Albert Einstein College of Medicine, Bronx, NY 10461, USA [3]Department of Biochemistry and Developmental Biology, Faculty of Medicine, University of Helsinki, Helsinki 00290, Finland

Abstract

Photoacoustic tomography (PAT) of genetically encoded probes allows imaging of targeted biological processes with high spatial resolution at depths. Here, we combined multi-scale photoacoustic imaging with, for the first time, a reversibly switchable non-fluorescent bacterial phytochrome BphP1. With a heme-derived biliverdin chromophore, BphP1 has the most red-shifted absorption among reported genetically encoded probes, and is reversibly photoconvertible between its red and near-infrared light absorption states. We combined single-wavelength PAT with efficient BphP1 photoswitching, enabling differential imaging that substantially removed background signals, enhanced detection sensitivity, increased penetration depth, and improved spatial resolution. In doing so, we monitored tumor growth and metastasis with a ~100 μm resolution at depths approaching 10 mm using photoacoustic computed tomography, and imaged individual cancer cells with a sub-optical-diffraction resolution of ~140 nm using photoacoustic microscopy. This technology is promising for biomedical studies at different length scales.

[6]Correspondence should be addressed to: V.V.V. (; Email: vladislav.verkhusha@einstein.yu.edu) and L.V.W. (; Email: lhwang@wustl.edu)

[4]Current address: Department of Mechanical and Biomedical Engineering, City University of Hong Kong, Tat Chee Avenue, Kowloon, Hong Kong, China

[5]These authors contributed equally

AUTHOR CONTRIBUTIONS

J.Y., V.V.V. and L.V.W. conceived and designed the study. J.Y., L.L. and L.W. constructed the imaging system. A.A.K. and D.M.S constructed the plasmids, purified and characterized the proteins *in vitro*, and established the stable bacterial and mammalian cell clones. J.Y., L.L. G.L., and R.Z. performed the photoacoustic experiments and analyzed the data. V.V.V and L.V.W. supervised the study. All authors wrote the manuscript.

COMPETING FINANCIAL INTERESTS

L.V. Wang has a financial interest in Endra, Inc., and Microphotoacoustics, Inc., which, however, did not support this work. The other authors declare no competing financial interests.

INTRODUCTION

Optical imaging has provided valuable information for biomedical studies[1, 2]. However, strong light scattering in tissue leads to a substantial tradeoff between the spatial resolution and penetration depth[3]. Photoacoustic (PA) tomography (PAT), on the other hand, breaks the depth and resolution limitations of pure optical imaging by acoustically detecting optical absorption contrast (Online Methods)[4]. The weak ultrasonic scattering in soft tissue provides PAT with highly scalable spatial resolution and penetration[5–11]. PAT is inherently suited for molecular imaging by using genetically encoded optical probes that are either fluorescent or not[12–15]. Genetically encoded optical probes with the following characteristics are highly desired in PAT: *(i)* Spectral properties that allow light penetration to deep tissues and robust unmixing from other endogenous biomolecules, *(ii)* light-sensing chromophores that are naturally present in tissues, *(iii)* orthogonality to mammalian cell metabolism. Fortunately, bacterial phytochromes (BphPs), among the very few light-sensing protein classes, can meet these criteria.

BphPs are photoreceptors sensitive to 600–800 nm light[16], a wavelength range that falls into the deep-penetration optical window in tissue[17]. BphPs consist of a photosensory core module and an output effector domain (Supplementary Fig. 1a). The spectral properties of BphPs are defined by a covalently attached chromophore, biliverdin IXα (BV) (Supplementary Fig. 1b)[18]. Inside a chromophore binding pocket, photoisomerization of BV leads to two conformational states, Pfr and Pr, resulting in absorption spectrum shift (Supplementary Fig. 1c)[19]. For unbound BV molecules in cells, photoisomerization occurs does not induce changes in the absorption spectrum (Supplementary Fig. 1d).

Here, we report a novel imaging approach, which, for the first time, combines PAT with a *Rp*BphP1 phytochrome from the bacterium *Rhodopseudomonas palustris* (termed below as BphP1). Two embodiments of PAT—photoacoustic computed tomography (PACT) and photoacoustic microscopy (PAM)[4]—were investigated at different length scales. Capitalizing on BphP1's reversible switching, we showed that this imaging approach dramatically enhanced the detection sensitivity of PACT at large depths. We demonstrated the high detection sensitivity *in vivo* by imaging the growth of BphP1-expressing tumors and monitoring the tumor metastases over prolonged periods of time. We extended this imaging approach to super-resolution PAM, achieving substantially finer spatial resolutions and higher image contrast.

RESULTS

Comparison of BphP1 with available genetically encoded probes

BphP1 has a natural photochromic behavior: it adopts a Pfr state as the ground state, and undergoes the Pfr→Pr photoconversion upon 730–790 nm light illumination and the Pr→Pfr photoconversion upon 630–690 nm light illumination. From here on, we choose the Pfr state of BphP1 as the ON state, and the Pr state as the OFF state, and used 780 nm light for Pfr→Pr photoconversion and 630 nm light for Pr→Pfr photoconversion. The molar extinction coefficients of the ON state BphP1 at 780 nm and of the OFF-state at 630 nm are respectively ~70-fold and ~40-fold higher than that of oxy-hemoglobin (HbO_2) (Fig. 1a,

Table 1). We compared BphP1 with the so far reported most red-shifted NIR fluorescent protein (FP), iRFP720, engineered from another BphP[20]. While the peak absorption of iRFP720 at 705 nm is comparable to that of the ON state BphP1 at 780 nm, iRFP720 is not photoswitchable (Supplementary Fig. 2a, Table 1). We also compared BphP1 with the so far reported most red-shifted photoswitchable FP, rsTagRFP, which can be photoswitched by altering light illumination between 440 nm and 570 nm[21, 22]. BphP1 was clearly advantageous over rsTagRFP for deep-tissue imaging because of its 2-fold higher extinction coefficient and ~200 nm red-shifted absorption (Supplementary Fig. 2a, Table 1).

We upgraded our whole-body PACT system to utilize BphP1 (Fig. 1b, **Online Methods**, Supplementary Video 1)[23]. We selected three wavelengths at 567 nm, 715 nm and 780 nm, based on the absorption spectra of the proteins and the power spectra of the lasers. Plastic tubes with purified proteins (~30 μM) were first immersed in water for PA imaging (Supplementary Fig. 2b). The laser fluence (8 mJ/cm^2) at all three wavelengths was within the ANSI safety limit for laser exposure (20 mJ/cm^2 at 567 nm; 40 mJ/cm^2 at 715 nm and 780 nm). The results clearly suggest the superior PA signal generation of ON state BphP1 at 780 nm (Fig. 1c). Purified proteins were then embedded at different depths in scattering media (1% intralipid and 10% gelatin in distilled water; reduced scattering coefficient of ~10 cm^{-1}) (Fig. 1d)[24]. The PA signal amplitude at 10 mm depth dropped by ~32-fold for BphP1 at 780 nm, ~101-fold for iRFP720 at 715 nm, and ~320-fold for rsTagRFP at 567 nm (Fig. 1e, Table 1). The noise equivalent detection concentration (NEC) was 2.0 ± 0.9 μM for BphP1 at 780 nm at 10 mm depth (Fig. 1f).

Characterization of reversible photoswitching of BphP1

Reversible photoswitching is an important feature of BphP1 for PAT, which enables differential imaging with a sensitivity, in principle, limited only by the noise level[14, 25, 26]. The photoswitching of BphP1 consists of a cis-trans photoisomerization of the D-ring of the biliverdin chromophore around its C15=C16 double bond (Supplementary Fig. 1c)[27]. Because the D-ring can rotate only in one direction, the intermediate conformations during the cis→trans and trans→cis photoswitching are different, resulting in different Pr→Pfr and Pfr→Pr photoswitching rates (Fig. 2a). Once BphP1 is photoswitched to the OFF state, it naturally relaxes back to the ON state with a half-life time of ~210 seconds. Multiple switching cycles did not cause photobleaching of BphP1. Because BphP1 photoswitching is a one-photon process, the photoswitching rate is approximately proportional to the switching light intensity (Fig. 2b), similar to photoswitchable FPs[21, 25, 28].

We evaluated photoswitching of BphP1 in scattering media at different depths using PACT (termed RS-PACT). Here, we define switching ratio as the ratio between the PA signal amplitudes measured in the ON and OFF states of BphP1. Each switching cycle began with 16 seconds of 780 nm light illumination for both PA imaging and switching off BphP1, followed by 16 seconds of 630 nm light illumination only for switching on the protein (Fig. 2c). During the first 3.2 seconds of a switching cycle, a 630 nm laser pulse was fired 72 μs after each 780 nm laser pulse to maintain the protein population in the ON state. We used the PA images acquired during the first and the last 3.2 seconds of the 780 nm light illumination as the ON state and OFF state images, respectively. Pixelwise subtraction of the OFF image

from the ON image generated a differential image. The switching wavelengths for other proteins were adjusted accordingly. Unless otherwise stated, a global threshold was applied to differential images, with a threshold level set at three times the noise level—estimated as the standard deviation of the background signal outside the imaged region.

HbO_2 and iRFP720 could not be photoswitched (Fig. 2d, Supplementary Fig. 3). rsTagRFP had a switching ratio of 8.5 ± 0.3 in clear media, but it essentially could not be photoswitched at depths beyond 3 mm, due to the strong light attenuation at 440 nm and 567 nm (Table 1). BphP1, however, maintained its photoswitching capability at 630 nm and 780 nm with increased depth, only reducing the switching ratio from 4.3 ± 0.2 in clear media to 2.8 ± 0.2 at 10 mm depth (Fig. 2d, Table 1). We imaged the three proteins at 10 mm depth with oxygenated whole bovine blood as a reference (Fig. 1d). We quantified the contrast (difference between proteins and blood) to noise ratio (CNR) of the ON state and differential PA images (Fig. 2e, Table 1). The differential PA image of BphP1 had ~21-fold enhancement in CNR than its ON state image (Fig. 2f). The red and NIR switching of BphP1 is clearly advantageous for deep PA imaging.

RS-PACT of BphP1 in mammalian cells and *in vivo*

We used U87 human glioblastoma cells to stably express BphP1 (**Online Methods**). Because BphP1 is non-fluorescent, we used a plasmid containing an internal ribosome entry site between BphP1 and EGFP. Both genes were translated from a single bicistronic mRNA (Supplementary Fig. 4a). We used the co-expressed EGFP to select stable BphP1-expressing cells, study the cytotoxicity of BphP1, and validate the PA imaging.

We imaged BphP1-expressing U87 cells embedded in scattering media (1% intralipid, 10% gelatin, and 2% oxygenated bovine blood in distilled water; absorption coefficient of 0.1 cm^{-1}; reduced scattering coefficient of ~10 cm^{-1}) at 10 mm depth using RS-PACT. The PA images acquired before and after the photoswitching both had strong background signals from blood, resulting in poor image contrast of the U87 cells (Supplementary Fig. 4b). By contrast, the differential image, averaged over 20 switching cycles, largely removed the non-switchable background signals and achieved a 50-fold enhancement in CNR (Supplementary Fig. 4c). Multiple switching cycles did not cause photobleaching of the cells (Supplementary Fig. 4d). We observed a noise-equivalent detection sensitivity of ~20 cells by using differential PA imaging (Fig. 3a).

We compared the new single-wavelength differential method with the traditional two-wavelength spectral unmixing method (Supplementary Fig. 5). The two-wavelength method, based on least-squares fitting, had low accuracy in identifying the cells, largely due to the unknown optical fluence inside the scattering phantom. By contrast, the single-wavelength differential method can extract the BphP1 signals with greater accuracy, achieving a 34-fold enhancement in CNR.

BphP1 has low cytotoxicity, similar to FPs engineered from various natural BphPs[20, 25]. First, we compared cell viability of the BphP1-expressing U87 cells with that of the wild-type U87 cells by annexin V staining. We observed no difference between the two types of cells (Supplementary Fig. 6a). Second, we monitored the BphP1-expressing U87 preclonal

cell culture for many generations. We did not observe decrease in the expression levels of BphP1 (measured by photoacoustic microscopy) and EGFP (measured by fluorescence cytometry) during several weeks of continuous cell culturing (Supplementary Figs. 6b–e).

By using RS-PACT, we imaged a mouse one week after injection of 10^6 BphP1-expressing U87 cells into the left kidney. Major organs, including the skin, kidneys, spleen, bladder, and spinal cord, could be delineated with strong signals from blood (Fig. 3b). The U87 tumor in the left kidney, overwhelmed by the blood signals, could not be detected. By contrast, after 20-cycle photoswitching, the differential PA image clearly showed the tumor at a depth up to ~8 mm, with an average CNR of ~20 (Fig. 3c). The photoswitchable tumor had different signals in the ON and OFF state images, while the non-switchable background signals from blood were virtually identical (Fig. 3d). After PA imaging, the tumor was histologically confirmed (Fig. 3e). RS-PACT was capable of three-dimensional (3D) imaging of a BphP1-expressing tumor (Supplementary Video 2). The superior sensitivity of BphP1-based RS-PACT was further demonstrated by comparing the images of a BphP1-expressing U87 tumor and a wild-type U87 tumor (Supplementary Fig. 7), and by imaging an otherwise undetectable U87 tumor in a mouse brain, at ~3 mm depth beneath the scalp surface (Fig. 3f, Supplementary Fig. 8).

Longitudinal RS-PACT of tumor metastases

We longitudinally imaged the growth of a BphP1-expressing U87 tumor in a mouse liver and monitored tumor metastases in the liver lobes for a month ($n = 6$) (Fig. 4a). The differential PA images detected the growth of a primary tumor in the right liver lobe, and later the secondary tumors resulted from metastatic spread to other liver lobes (Fig. 4a). The smallest secondary tumor had an average diameter of ~300 μm. Assuming that the mean diameter of U87 cells is ~10 μm, each resolution voxel of the secondary tumor corresponds to ~3000 U87 cells. The CNR of the above-mentioned tumor is ~15 in the differential image, suggesting it is possible to detect as few as ~200 cells at this depth. Over one month, we observed an exponential growth of the primary tumor, and a delayed exponential growth of the secondary tumor (Fig. 4b). There was no difference between the growth rates of the primary tumor (from day 0) and secondary tumors (from day 7). The cross-sectional area doubling times of the primary tumor and secondary tumors are respectively 8.0 ± 1.2 days and 7.2 ± 2.7 days, suggesting cell doubling times of 5.3 ± 0.8 days and 4.8 ± 1.8 days. After the PA imaging, we histologically confirmed the relative locations of the tumors (Fig. 4c).

Sub-diffraction photoacoustic microscopy of BphP1

By tightly focusing the excitation light, PAT has provided optically-determined spatial resolution on the scale of micrometers, a technology referred to as optical-resolution photoacoustic microscopy (PAM)[4]. Here, we demonstrate that BphP1 can improve the image contrast of optical-resolution PAM *in vivo*, and more importantly, break the optical-diffraction limit for super-resolution PA imaging.

We developed a double-illumination PAM that illuminates the object from above and below (Fig. 5a, **Online Methods**). The top illumination utilizes a 0.1 numerical aperture (NA)

objective, and the bottom illumination uses a 1.4 NA oil-immersion objective. Because of its relatively large depth of focus (~83 μm), the top illumination is suited for *in vivo* imaging with capillary-level resolution (~3 μm). As a demonstration, we imaged a nude mouse ear bearing BphP1-expressing U87 tumors, where the differential image had a ~67-fold greater CNR than the ON state image (Supplementary Fig. 9).

Moreover, we developed sub-diffraction PA imaging based on the reversible photoswitching of BphP1 (termed RS-PAM) (Fig. 5b, **Online Methods**, and Supplementary Notes 1–3). Briefly, when a train of Gaussian-shaped laser pulses at 780 nm repeatedly strike a group of ON-state BphP1 molecules, the PA signals generated by the consecutive laser pulses decrease, as more and more BphP1 molecules are inhomogeneously switched off at a rate proportional to the local excitation intensity (Supplementary Note 1). The PA signal from the center of the excitation spot decays faster than that from the periphery. The detected PA signal decay is integrated over all the molecules in the excitation spot. When a polynomial function is used to fit the signal decay as a function of time, the high-order coefficient of the fitted polynomial imposes non-linear weighting on the signal contributions from the excitation spot, accentuating the contribution from the center (Supplementary Note 2). A higher-order coefficient has a narrower spatial distribution. RS-PAM extracts the highest-order coefficient of the polynomial fitting at each pixel as its image contrast, achieving sub-diffraction spatial resolution[29]. Note that the highest-order coefficient that can be effectively extracted is determined by the signal-to-noise ratio of the original PA signal decay. Importantly, by efficiently blocking the out-of-focus signals, RS-PAM provides optical-sectioning capability for laterally large targets (Supplementary Note 3), which is not available in conventional PAM[30].

Using the bottom illumination of the PAM system, we demonstrated sub-diffraction lateral resolution by imaging a monolayer of BphP1-expressing bacteria densely fixed on a cover glass. At each pixel, one hundred laser pulses at 780 nm were used to record the switching-off dynamics of BphP1. The OFF-state BphP1 molecules were then switched back on with 1 second of continuous-wave illumination at 630 nm. Compared to the conventional PAM image, the RS-PAM image showed superior lateral resolution, enabling better separation of neighboring bacteria (Fig. 5c–e). RS-PAM has achieved a lateral resolution of ~141 nm, ~2-fold finer than that of conventional PAM (Supplementary Fig. 10a).

We demonstrated the axial resolution of RS-PAM on a multilayer of fixed BphP1-expressing U87 cells (total thickness: ~35 μm). For laterally large targets, conventional PAM exhibits poor axial resolution (~30 μm) as a result of the time-resolved acoustic detection (Supplementary Fig. 10b), and therefore was not able to resolve different layers of U87 cells (Supplementary Fig. 11). In comparison, RS-PAM was able to block the PA signals generated by the out-of-focus cells and consequently achieved thin optical sectioning of ~0.4 μm, ~75-fold finer than that of conventional PAM (Supplementary Fig. 10b). By a depth scanning, RS-PAM clearly resolved U87 cells at different layers (Fig. 5f–g, Supplementary Fig. 11, Supplementary Video 3).

DISCUSSION

We have developed photoacoustic tomography that, for the first time, combines deep-tissue PA imaging with a non-fluorescent photochromic NIR bacterial phytochrome, BphP1. With this new imaging technology, we have achieved a PA detection sensitivity of tens to hundreds of live mammalian cells at a centimeter depth. Moreover, PA imaging of BphP1 has enhanced the image contrast of optical-resolution PAM *in vivo* and achieved sub-diffraction imaging of individual cells.

The above achievements come from BphP1's unique photochemical features. First, BphP1 has two red- and NIR-absorbing photoconvertible states, enabling deep-tissue PA imaging and photoswitching[20]. Second, BphP1 is non-cytotoxic and it does not affect cell metabolism. Third, BphP1 efficiently and specifically binds endogenous chromophore BV, and does not require an exogenous supply. Mammalian cells in different organs generally have sufficient BV for BphP1 binding. Fourth, BphP1 exhibits low photoswitching fatigue during photoconversion, allowing longitudinal imaging.

Meanwhile, PAT is inherently suited to take maximum advantage of BphP1's photochemical features. First, PAT can provide high-resolution imaging of BphP1 at depths beyond that achieved by pure optical techniques[26]. Second, in comparison to the traditional multi-wavelength methods[31], single-wavelength imaging at 780 nm much reduces the influence of unknown local light fluence (J/cm^2) on extracting the protein signals. The wavelength-dependent local light fluence is affected by not only the optical attenuation of the intervening tissue but also the local optical absorption[31, 32]. Third, due to the relatively low light attenuation in the red and NIR regions, the switching efficiency of BphP1 can be maintained in deep tissue. Lastly, the differential imaging process is simple and reliable. The background signals are removed without sacrificing either the spatial resolution or sensitivity[12, 31].

We have carefully mitigated potential artifacts in our differential images. First, BphP1-expressing cells had relatively weak absorption. The photoswitching of the cells had negligible influence on the total internal optical fluence distribution. Second, for *in vivo* imaging, animal motion was largely reduced by the specially designed animal mounting methods (Online Methods). Image averaging over multiple switching cycles further reduced motion artifacts. Third, the laser pulse energy fluctuation was less than 3%, and its effect was further minimized by multiplexed data acquisition and multi-cycle averaging. Finally, signal thresholding removed remaining artifacts.

Further development of the technology may include improvement of the NIR photochromic probes, either by engineering the BphP1 properties[16] or by seeking better BphPs in nature[18]. Relatively inexpensive continuous-wave laser diodes can be used for photoswitching[33]. The current PACT has a relatively low imaging speed (32 seconds per switching cycle and 11 minutes with 20 averaging cycles). The imaging speed can be improved by using a 50 Hz laser and a 512-channel data acquisition system, which can avoid the data multiplexing and thus reduce the imaging time.

Overall, BphP1-based PAT opens new possibilities for biomedical applications. For example, transgenic mouse models that express BphP1 in neurons can be used for longitudinal PA monitoring of neural network development[34]. BphP1-expressing cardiomyocytes should allow direct PA imaging of heart activities, which is otherwise challenging due to the large amount of blood inside the heart. The high detection sensitivity of BphP1 will be useful for capturing non-pigmented cancer cells circulating in the blood stream in deep tissue[35], as well as for cell tracking in immunotherapy[36].

ONLINE METHODS

Photoacoustic tomography (PAT)

In PAT, as photons propagate in tissue, some are absorbed by biomolecules, and their energy is partially or completely converted into heat. The heat-induced pressure propagates in tissue and is detected outside the tissue by an ultrasonic transducer or transducer array to form an image that maps the original optical energy deposition in the tissue. Based on the image formation methods, PAT has two major implementations. The first, direct image formation, is based on mechanical scanning of a focused single-element ultrasonic transducer, and is commonly used in photoacoustic microscopy (PAM). The second, reconstruction image formation, is based on parallel detection by an unfocused multi-element ultrasonic transducer array or a mechanical/electronic scanning equivalent, and is used in photoacoustic computed tomography (PACT).

Plasmid construction and protein expression

The *Rp*BphP1 gene was kindly provided by E. Giraud. For mammalian expression, the BphP1 gene was PCR amplified as *Nhe*I-*Bgl*II fragments and cloned into multi cloning sites of the pIRES2-EGFP vector (Takara-Clontech), allowing co-expression of BphP1 and EGFP proteins separately but from the same bicistronic mRNA. For bacterial expression of BphP1, the pBAD/His-B vector (Life Technologies-Invitrogen) was used.

rsTagRFP and iRFP720 were purified from *E. coli* bacteria as described before[20, 21]. BphP1 with a polyhistidine tag at the N-terminus was expressed in LMG194 bacterial cells (Life Technologies-Invitrogen) containing a pWA23h plasmid encoding heme oxygenase for BV synthesis in *E. coli*[20, 25]. The bacterial cells were grown in RM medium supplemented with ampicillin, kanamycin, and 0.02% rhamnose for 6–8 h, followed by induction of protein expression by adding 0.002% arabinose. The proteins were purified using a Ni-NTA agarose (Qiagen).

Absorption spectra of BphP1, dissolved in phosphate buffered saline, were measured using a standard spectrophotometer (Hitachi U-2000) with a 100 μL quartz microcuvette (Starna Cells). The spectrum of the ON state BphP1 was measured without a photoswitching light source, because the ON state is the ground state (or natural state). To measure the OFF state spectrum, photoswitching was performed with a 780/25 nm LED placed above the microcuvette. The photoswitching beam direction was orthogonal to the optical beam path of the spectrophotometer. The OFF state spectrum was measured after the photoswitching was completed and the LED was turned off, so there was no interference with the

measurements. Because of the extremely low light intensity (<1 μW/cm^2), changes in the absorption spectra of BphP1 induced by the light illumination inside the spectrophotometer were negligible.

The photoswitching of BphP1 in Figure 2a was performed by using 780/25 nm and 630/25 nm LEDs, which were mounted orthogonal to the optical beam path of the spectrophotometer to avoid detection interference. BphP1 was photoswitched directly in the 100 μL quartz microcuvette of the spectrophotometer, while its absorbance at 780 nm was measured.

Mammalian cell culture

U87 cells were grown in DMEM medium supplemented with 10% FBS, penicillin-streptomycin mixture, 2 mM glutamine (all from Life Technologies-Invitrogen) at 37°C in 5% CO_2 air atmosphere. U87 stable preclonal mixture was obtained by transfecting cells with pBphP1- IRES2-EGFP plasmid. Plasmid transfection was performed using an Effectene reagent (Qiagen). Cells were further selected with 700 μg/ml of G418 antibiotic for two weeks and enriched using a FACSAria sorter (BD Biosciences) equipped with a 488 nm laser and a 530/30 nm emission filter. For further culturing of U87 cells stably expressing BphP1, the medium was additionally supplemented with 500 μg/ml of G418 (Corning). To implant xenograph tumors into the animal (brain, kidney or liver), about 10^6 U87 cells, either stably expressing BphP1 or un-modified, in 0.2 mL PBS were injected into mice with the guidance of a commercial ultrasound system (Vevo LAZR, Visualsonics). For photoacoustic microscopy with sub-diffraction resolution, U87 cells were plated into a 35 mm glass-bottom petri dish (P35GCOL-0-14-C, MatTek).

Expression level of EGFP during prolonged culturing of BphP1-expressing U87 preclonal cell mixture was measured using a LSRII flow cytometer (BD Biosciences) equipped with a 488 nm laser and a 530/40 nm emission filter. For cell viability assay, wild-type U87 cells and BphP1-expressing U87 cells were stained with annexin V conjugated with allophycocyanin dye according to manufacturer's protocol (BD Biosciences). Cells were analyzed using the LSRII flow cytometer equipped with a 640 nm laser and 660/20 nm emission filter. The cell viability was estimated by the percentage of annexin V negative cells. Typically, the cell samples were triplicated, and at least 10^4 cells were analyzed per sample.

Animal preparation

Adult, two- to three-month-old nude mice (Hsd:Athymic Nude-Foxl^{NU}, Harlan Co.; body weight: ~20−30 g; female) were used for all *in vivo* experiments. All experimental procedures were carried out in conformity with laboratory animal protocols approved by the Animal Studies Committee at the Washington University in St. Louis. Throughout the experiment, the mouse was maintained under anesthesia with 1.5% vaporized isoflurane. The mouse was taped to a lab-made motorized animal holder, which held the animal upright during imaging. The top of the holder was a small aluminum tube affixed to the animal's nose and mouth, and the bottom was an aluminum cylinder attached to a permanent magnet. The magnet securely held the animal holder to the scanning stage for elevational scanning.

The animal's fore and hind legs were taped to the top and bottom parts of the holder, respectively. The two parts were connected by four lengths of high-strength fishing line (0.13 mm diameter braided line). The combination of the magnet and a counterweight put the thin lines in tension to minimize holder movement caused by animal respiratory motion[23]. The animal's trunk was immersed in water, and its body temperature was maintained at 37 °C by circulating the water through a heating bath outside the tank.

Hematoxylin and eosin (H&E) histology and fluorescence imaging

The tumor-bearing kidney and liver were harvested and fixed in 4% paraformaldehyde for 24 h. Coronal sections (5 μm thick) were cut with paraffin embedding. Standard H&E staining was performed on the sections, which were examined using bright-field microscopy (NanoZoomer, Hamamatsu) with a 20× objective (NA = 0.67).

The harvested tissue and the BphP1-expressing U87 cells were also imaged by wide-field fluorescence microscopy (Fluoview 1000, Olympus), using the co-expressed EGFP protein (excitation wavelength: 488 nm; emission filter wavelength: 510 nm). A 4× objective (NA = 0.10) was used to image the harvested tissue, and a 20× objective (NA = 0.70) was used to image the cells.

Whole-body photoacoustic computed tomography of reversibly switchable phytochrome BphP1 (RS-PACT)

The whole-body photoacoustic computed tomography system has been upgraded from our previous work[23] (Fig. 1b). In order to image BphP1 and other control proteins, we have combined a Ti:Sapphire laser (LS-2137/LT-2211A, LOTIS) and a lab-made optical parametric oscillator (OPO) laser, each pumped by an Nd:YAG laser with a 10 Hz pulse repetition rate. The 780 nm light from the Ti:Sapphire laser is used for both whole-body PA imaging and switching off BphP1 at the same time, while the 630 nm light from the OPO laser is used for switching on the protein. The flashlamps of the two pump lasers are synchronized, and the two lasers are individually triggered by an FPGA-based controller (sbRIO9323, National Instruments). The two laser beams are combined by a dichroic mirror, and their incident fluences (in mJ/cm^2) are measured by an optical power meter. The laser beam is first homogenized by an optical diffuser (EDC-5, RPC Photonics), and then passed through a conical lens (cone angle 130 °, Delmar Photonics) to form a ring-shaped light pattern. The light is then passed through an optical condenser to form a ring-shape light band around the animal's trunk. The light incident area is aligned slightly above the acoustic focal plane to ensure sufficient light diffusion. The thickness of the light band is ~5 mm, and its diameter is similar to the cross-sectional diameter (~2−3 cm) of a mouse. The maximum light fluence on the skin of the animal is ~8 mJ/cm^2, which is well below the American National Standards Institute (ANSI) safety limit.

The photoacoustic signals are detected by a full-ring ultrasonic transducer array (Imasonic) with a 5 cm diameter, 5 MHz central frequency, more than 80% one-way bandwidth, and 512 elements. Each element (10 mm height, 0.3 mm pitch, and 0.1 mm inter-element space) is cylindrically focused to produce an axial focal distance of 19.8 mm (acoustic numerical aperture: 0.25). The combined foci of all 512 elements form an approximately uniform

imaging region with a 20 mm diameter and 1 mm thickness. Within this region, the radial resolution is 100 μm, and the tangential resolution is 100–250 μm, where the tangential direction is perpendicular to the radial direction. The tangential resolution depends on the radial distance from the center and degrades slowly with the radial distance. The data acquisition system has 64 channels with 8-fold multiplexing. The cross-sectional imaging speed is 1.6 s per frame. For image reconstruction, the raw data from each element is first Wiener deconvolved to account for the ultrasonic transducer's impulse response and then reconstructed within each imaging plane, based on the universal back-projection algorithm[37]. To mitigate the artifacts induced by acoustic heterogeneities in the animal body, such as air cavities in gastrointestinal tract and backbone, the half-time image reconstruction algorithm is applied in combination with the universal back-projection reconstruction[38].

Sub-diffraction photoacoustic microscopy of reversibly switchable phytochrome BphP1 (RS-PAM)

As shown in Fig. 5a, a pulsed Nd:YLF laser (INNOSLAB, 523 nm, Edgewave) pumps a dye laser (CBR-D, Sirah) to provide 780 nm light for PA imaging and switching off BphP1. A CW 630 nm laser diode (Information Unlimited Inc.) switches on the protein. The light beams are combined by a dichroic mirror, reshaped by an iris (ID25SS, Thorlabs) and attenuated by a neutral density filter (NDC-50C-2M, Thorlabs). The attenuated beam is then split into two sub-beams (top and bottom) by a 50/50 beam splitter (BSW04, Thorlabs). The top beam is focused by a condenser lens (LA1131, Thorlabs) before passing through a 50 μm pinhole (P50C, Thorlabs) for further spatial filtering. The filtered beam is then focused by an optical objective (AC127-050-A, Thorlabs. NA: 0.1 in air) into the object from the top. A beam combiner composed of a thin layer of silicone oil sandwiched by a right-angle prism (NT32-545, Edmund Optics) and a rhomboid prism (NT49-419, Edmund Optics) provides acoustic-optical coaxial alignment. The resultant photoacoustic waves are detected by an ultrasonic transducer (V214-BB-RM, Olympus-NDT) with a central frequency of 50 MHz. An acoustic lens with a 0.5 NA is ground into the bottom of the rhomboid prism to provide an acoustic focal diameter of 30 μm. An optical correction lens is attached to the top of the beam combiner to correct aberration. The acoustic lens is submerged in a water-tank for ultrasound coupling. The bottom beam duplicates the same path as the top beam, except that it is directly focused into the object from the bottom without going through the beam combiner and water-tank. The bottom objective has a 1.4 NA with oil immersion (MPLAPON100XO, Olympus). By carefully adjusting the positions of the two objectives, we achieve a confocal configuration of the two optical foci and the acoustic focus. Volumetric imaging is acquired by two-dimensional raster scanning of the object. A photodiode is added to monitor the fluctuations of the laser pulse energy.

The mechanism of the lateral resolution enhancement of RS-PAM is illustrated in Fig. 5b. The mathematical details are elaborated in Supplementary Notes 1–3. The effective lateral point spread function (PSF) of the system is $\frac{0.51}{\sqrt{1+bm}}\frac{\lambda_0}{\mathrm{NA}}$, where b is the power dependence of the switching-off rate on the excitation intensity (b=1 for Bphp1), m is the order of polynomial fitting of the signal decay (m=3 in this study), λ_0 is the excitation wavelength,

and NA is the numerical aperture of the objective[29]. The lateral resolution of RS-PAM is finer than that of conventional PAM by a factor of $\sqrt{1+bm}$.

In addition to the sub-diffraction lateral resolution, the nonlinear nature of the RS-PAM signal enables optical sectioning in the axial direction, which is of particular interest for large (or planar) targets. Compared with the in-focus molecules, the out-of-focus molecules are less affected during the switching-off process. Therefore, high-order coefficients extracted from the polynomial fitting of the signal decay contain mainly in-focus contributions, and thus RS-PAM achieves optical sectioning. Like the lateral resolution enhancement, the optical-sectioning strength of RS-PAM is determined by the power dependence of the switching-off rate on the excitation intensity. For point targets, RS-PAM can achieve an axial resolution of $1.8\sqrt{2^{1/(1+bm)}-1}\frac{\lambda_0}{\mathrm{NA}^2}$[30]. For large targets, RS-PAM can achieve an axial resolution of $1.8\sqrt{2^{1/bm}-1}\frac{\lambda_0}{\mathrm{NA}^2}$.

Reproducibility

The experiments were not randomized. The investigators were not blinded to allocation during experiments and outcome assessment. No sample-size estimation was performed to ensure adequate power to detect a prespecified effect size.

Supplementary Material

Refer to Web version on PubMed Central for supplementary material.

ACKNOWLEDGEMENTS

We thank E. Giraud (Institute for Research and Development, France) for the *Rp*BphP1 gene, A. Krumholz and J. Shi for the technical support, J. Ballard for the reading of the manuscript, and Alafi Neuroimaging Laboratory for the bright-field microscopy. This work was sponsored by the US National Institutes of Health grants DP1 EB016986 (NIH Director's Pioneer Award), R01 CA186567 (NIH Director's Transformative Research Award), U01 NS090579 (BRAIN Initiative), R01 EB016963, S10 RR026922 (all to L.V.W.), and GM073913, GM108579, CA164468 and by the EU FP7 grant ERC-2013-ADG-340233 (all to V.V.V.), and by the Neuroscience Blueprint Center Core grant NS057105 (to Alafi Neuroimaging Laboratory).

REFERENCES

1. Ntziachristos V. Going deeper than microscopy: the optical imaging frontier in biology. Nat Methods. 2010; 7:603–614. [PubMed: 20676081]
2. Weissleder R, Pittet MJ. Imaging in the era of molecular oncology. Nature. 2008; 452:580–589. [PubMed: 18385732]
3. Rice WL, Shcherbakova DM, Verkhusha VV, Kumar ATN. In Vivo Tomographic Imaging of Deep-Seated Cancer Using Fluorescence Lifetime Contrast. Cancer Research. 2015; 75:1236–1243. [PubMed: 25670171]
4. Wang LHV, Hu S. Photoacoustic Tomography: In Vivo Imaging from Organelles to Organs. Science. 2012; 335:1458–1462. [PubMed: 22442475]
5. Brecht HP, et al. Whole-body three-dimensional optoacoustic tomography system for small animals. J Biomed Opt. 2009; 14:064007. [PubMed: 20059245]
6. Kruger RA, Lam RB, Reinecke DR, Del Rio SP, Doyle RP. Photoacoustic angiography of the breast. Medical Physics. 2010; 37:6096–6100. [PubMed: 21158321]

7. de la Zerda A, Kim JW, Galanzha EI, Gambhir SS, Zharov VP. Advanced contrast nanoagents for photoacoustic molecular imaging, cytometry, blood test and photothermal theranostics. Contrast Media & Molecular Imaging. 2011; 6:346–369. [PubMed: 22025336]
8. Luke GP, Yeager D, Emelianov SY. Biomedical Applications of Photoacoustic Imaging with Exogenous Contrast Agents. Annals of Biomedical Engineering. 2012; 40:422–437. [PubMed: 22048668]
9. Kircher MF, et al. A brain tumor molecular imaging strategy using a new triple-modality MRI-photoacoustic-Raman nanoparticle. Nat Med. 2012; 18 829-U235.
10. Wang XD, et al. Noninvasive laser-induced photoacoustic tomography for structural and functional in vivo imaging of the brain. Nature Biotechnology. 2003; 21:803–806.
11. Zhang HF, Maslov K, Stoica G, Wang LHV. Functional photoacoustic microscopy for high-resolution and noninvasive in vivo imaging. Nature Biotechnology. 2006; 24:848–851.
12. Razansky D, et al. Multispectral opto-acoustic tomography of deep-seated fluorescent proteins in vivo. Nature Photonics. 2009; 3:412–417.
13. Krumholz A, Shcherbakova DM, Xia J, Wang LV, Verkhusha VV. Multicontrast photoacoustic in vivo imaging using near-infrared fluorescent proteins. Sci Rep. 2014; 4:3939. [PubMed: 24487319]
14. Stiel AC, et al. High-contrast imaging of reversibly switchable fluorescent proteins via temporally unmixed multispectral optoacoustic tomography. Opt Lett. 2015; 40:367–370. [PubMed: 25680049]
15. Jathoul AP, et al. Deep in vivo photoacoustic imaging of mammalian tissues using a tyrosinase-based genetic reporter. Nat Photon. 2015; 9:239–246.
16. Piatkevich KD, Subach FV, Verkhusha VV. Engineering of bacterial phytochromes for near-infrared imaging, sensing, and light-control in mammals. Chem Soc Rev. 2013; 42:3441–3452. [PubMed: 23361376]
17. Weissleder R, Ntziachristos V. Shedding light onto live molecular targets. Nat Med. 2003; 9:123–128. [PubMed: 12514725]
18. Giraud E, Vermeglio A. Bacteriophytochromes in anoxygenic photosynthetic bacteria. Photosynth Res. 2008; 97:141–153. [PubMed: 18612842]
19. Auldridge ME, Forest KT. Bacterial phytochromes: more than meets the light. Crit Rev Biochem Mol Biol. 2011; 46:67–88. [PubMed: 21250783]
20. Shcherbakova DM, Verkhusha VV. Near-infrared fluorescent proteins for multicolor in vivo imaging. Nat Methods. 2013; 10:751–754. [PubMed: 23770755]
21. Subach FV, et al. Red Fluorescent Protein with Reversibly Photoswitchable Absorbance for Photochromic FRET. Chem Biol. 2010; 17:745–755. [PubMed: 20659687]
22. Pletnev S, Subach FV, Dauter Z, Wlodawer A, Verkhusha VV. A structural basis for reversible photoswitching of absorbance spectra in red fluorescent protein rsTagRFP. J Mol Biol. 2012; 417:144–151. [PubMed: 22310052]
23. Xia J, et al. Whole-body ring-shaped confocal photoacoustic computed tomography of small animals in vivo. J Biomed Opt. 2012; 17:050506. [PubMed: 22612121]
24. Lai PX, Xu X, Wang LHV. Dependence of optical scattering from Intralipid in gelatin-gel based tissue-mimicking phantoms on mixing temperature and time. Journal of Biomedical Optics. 2014; 19:035002.
25. Piatkevich KD, Subach FV, Verkhusha VV. Far-red light photoactivatable near-infrared fluorescent proteins engineered from a bacterial phytochrome. Nat Commun. 2013; 4:2153. [PubMed: 23842578]
26. Yan Y, Marriott ME, Petchprayoon C, Marriott G. Optical switch probes and optical lock-in detection (OLID) imaging microscopy: high-contrast fluorescence imaging within living systems. Biochem J. 2011; 433:411–422. [PubMed: 21235524]
27. Toh KC, Stojkovic EA, van Stokkum IH, Moffat K, Kennis JT. Proton-transfer and hydrogen-bond interactions determine fluorescence quantum yield and photochemical efficiency of bacteriophytochrome. Proc Natl Acad Sci USA. 2010; 107:9170–9175. [PubMed: 20435909]

28. Habuchi S, et al. Reversible single-molecule photoswitching in the GFP-like fluorescent protein Dronpa. Proceedings of the National Academy of Sciences of the United States of America. 2005; 102:9511–9516. [PubMed: 15972810]
29. Yao JJ, et al. Reversibly switchable fluorescence microscopy with enhanced resolution and image contrast. J Biomed Opt. 2014; 19:086018. [PubMed: 25144452]
30. Yao JJ, Wang LD, Li CY, Zhang C, Wang LHV. Photoimprint Photoacoustic Microscopy for Three-Dimensional Label-Free Subdiffraction Imaging. Physical Review Letters. 2014; 112:014302. [PubMed: 24483902]
31. Deliolanis NC, et al. Deep-tissue reporter-gene imaging with fluorescence and optoacoustic tomography: a performance overview. Mol Imaging Biol. 2014; 16:652–660. [PubMed: 24609633]
32. Ntziachristos V, Razansky D. Molecular Imaging by Means of Multispectral Optoacoustic Tomography (MSOT). Chemical Reviews. 2010; 110:2783–2794. [PubMed: 20387910]
33. Xia J, Wang LHV. Small-Animal Whole-Body Photoacoustic Tomography: A Review. Ieee Transactions on Biomedical Engineering. 2014; 61:1380–1389. [PubMed: 24108456]
34. Devor A, et al. The Challenge of Connecting the Dots in the BRAIN. Neuron. 2013; 80:270–274. [PubMed: 24139032]
35. Chaffer CL, Weinberg RA. A Perspective on Cancer Cell Metastasis. Science. 2011; 331:1559–1564. [PubMed: 21436443]
36. Couzin-Frankel J. Cancer Immunotherapy. Science. 2013; 342:1432–1433. [PubMed: 24357284]
37. Xu MH, Wang LHV. Universal back-projection algorithm for photoacoustic computed tomography. Physical Review E. 2005; 71:7.
38. Anastasio MA, et al. Half-time image reconstruction in thermoacoustic tomography. Ieee Transactions on Medical Imaging. 2005; 24:199–210. [PubMed: 15707246]

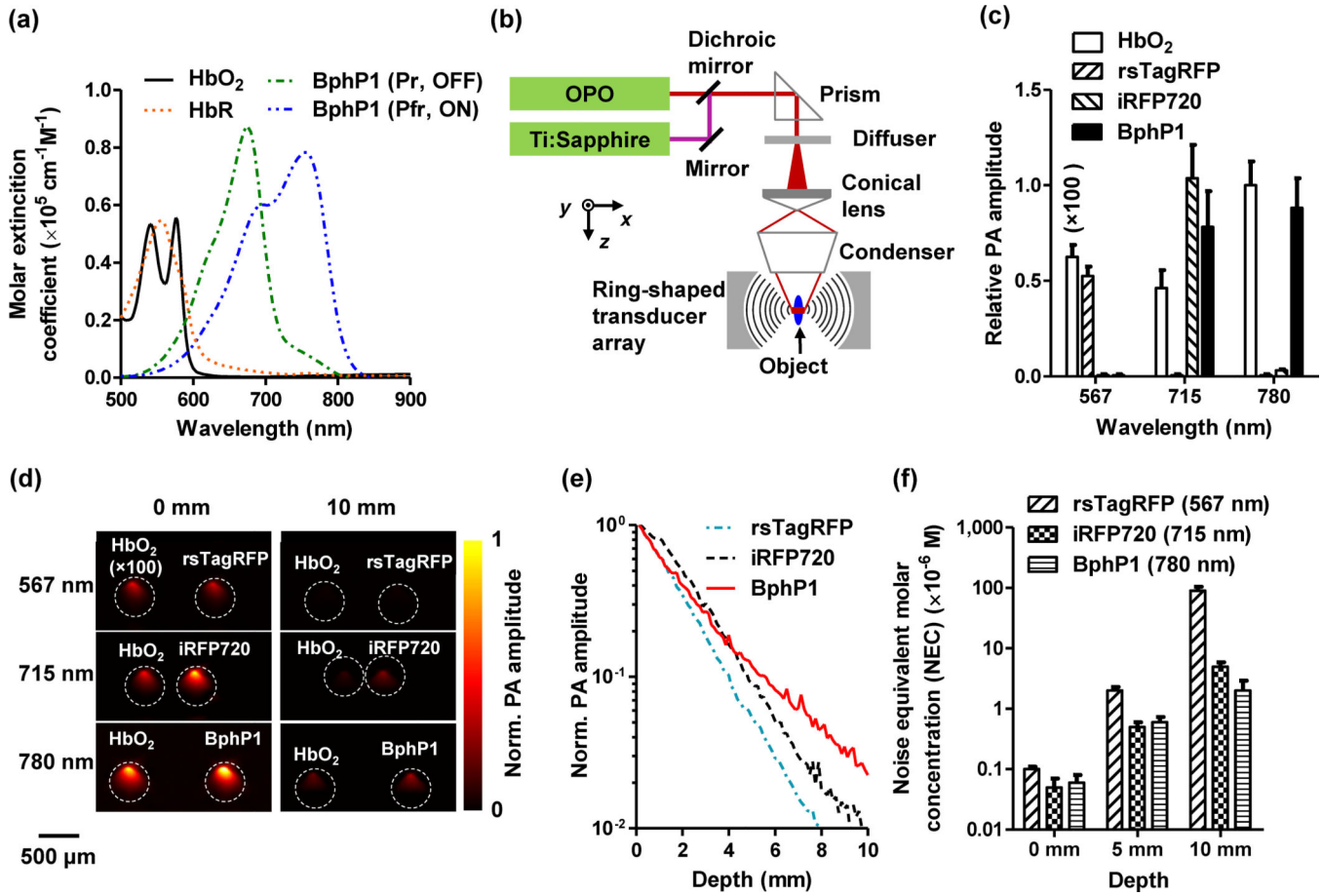

Fig. 1.

Optical and photoacoustic characterization of the non-fluorescent bacterial phytochrome BphP1. (a) Molar extinction spectra of oxy-hemoglobin (HbO_2), deoxy-hemoglobin (HbR), Pfr (ON) and Pr (OFF) state BphP1. (b) Schematic of the whole-body photoacoustic computed tomography (PACT) system with a ring-shaped illumination pattern. The Ti:Sapphire laser at 780 nm is used for PA imaging and switching off BphP1. The optical parametric oscillator (OPO) laser at 630 nm is used for switching on BphP1. (c) PA signal amplitudes of 30 μM purified ON state rsTagRFP, iRFP720, and ON state BphP1 in clear media, acquired at 567 nm, 715 nm and 780 nm. HbO_2 concentration was 2.3 mM for the measurement at 715 nm and 780 nm, and was diluted to 23 μM for the measurement at 567 nm. All the PA signal amplitudes were normalized by that of HbO_2 acquired at 780 nm. Error bars, s.d. (d) PA images of transparent plastic tubes filled with proteins in clear media (left column) and with addition of 10 mm thick scattering media (right column). (e) PA signal of purified proteins acquired with increasing imaging depth up to 10 mm in scattering media. (f) Noise-equivalent detectable concentrations of purified proteins at different depths, acquired at their respective absorbing wavelengths. Error bars, s.d.

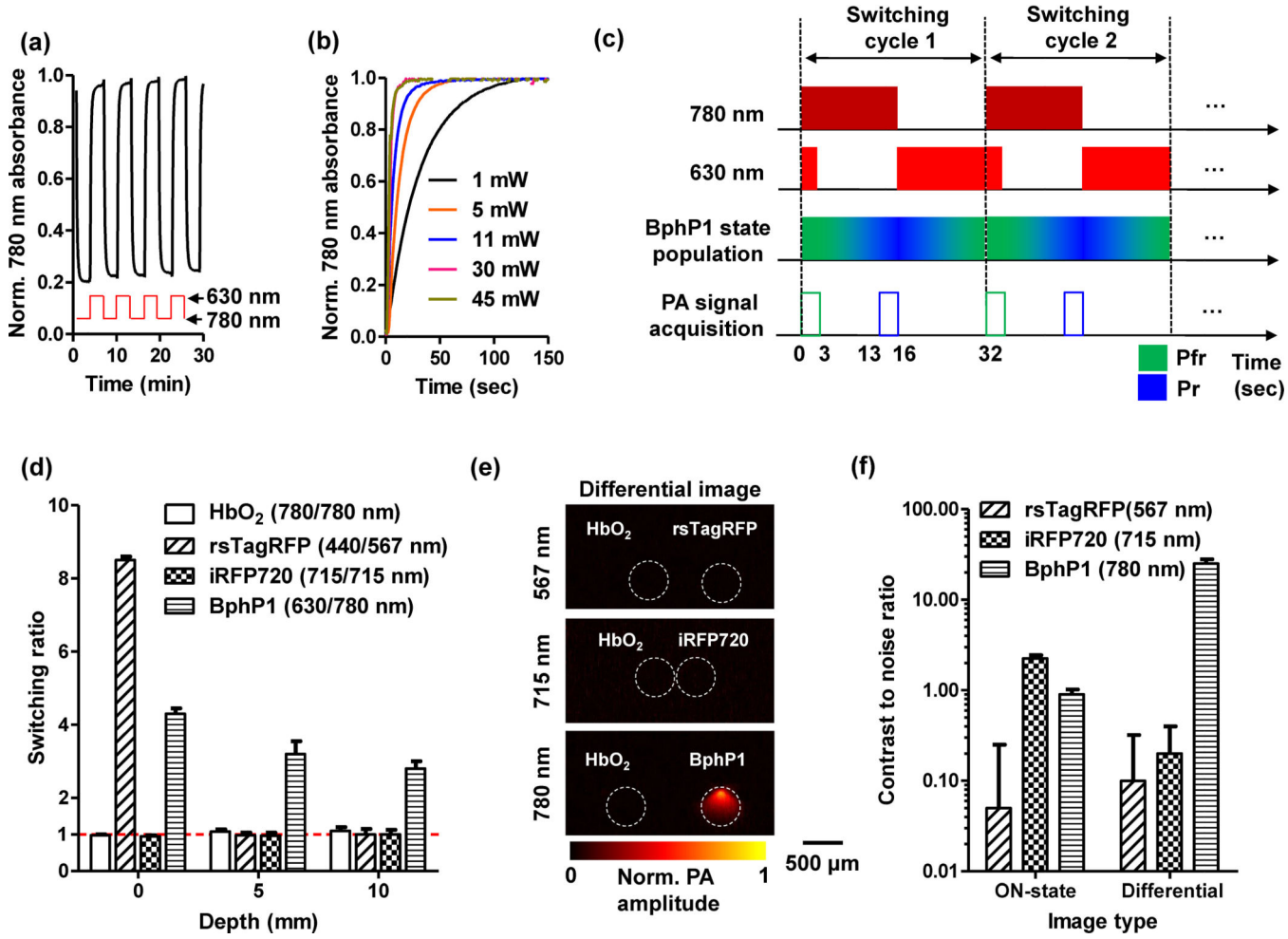

Fig. 2.

Optical and photoacoustic (PA) characterization of reversible photoswitching of BphP1. (a) Absorbance of BphP1 at 780 nm, switched off with 780 nm light illumination and then switched on with 630 nm light illumination. The photoswitching period was 180 seconds for both wavelengths, with an absorbance-rise half-time of 16 seconds and an absorbance-fall half-time of 8 seconds. (b) Switching on rate of BphP1 with 630 nm light illumination at different power levels. (c) Time sequences of the photoswitching cycle of BphP1. The 780 nm light is used for PA imaging and switching off the protein, and. The PA signals are acquired only with the 780 nm illumination. (d) Switching ratio of purified proteins at different imaging depths in scattering media (1% intralipid and 10% gelatin in distilled water; reduced scattering coefficient of ~10 cm^{-1}). We define switching ratio as the ratio between the PA signal amplitudes acquired in the ON and OFF states of the proteins. Error bars, s.d. (e) Differential PA images of the purified proteins at 10 mm depth, acquired at their respective wavelengths. HbO_2 was imaged with each protein to provide a reference. (f) Comparison of the contrast to noise ratio quantified from the ON state images and the differential images. Error bars, s.d.

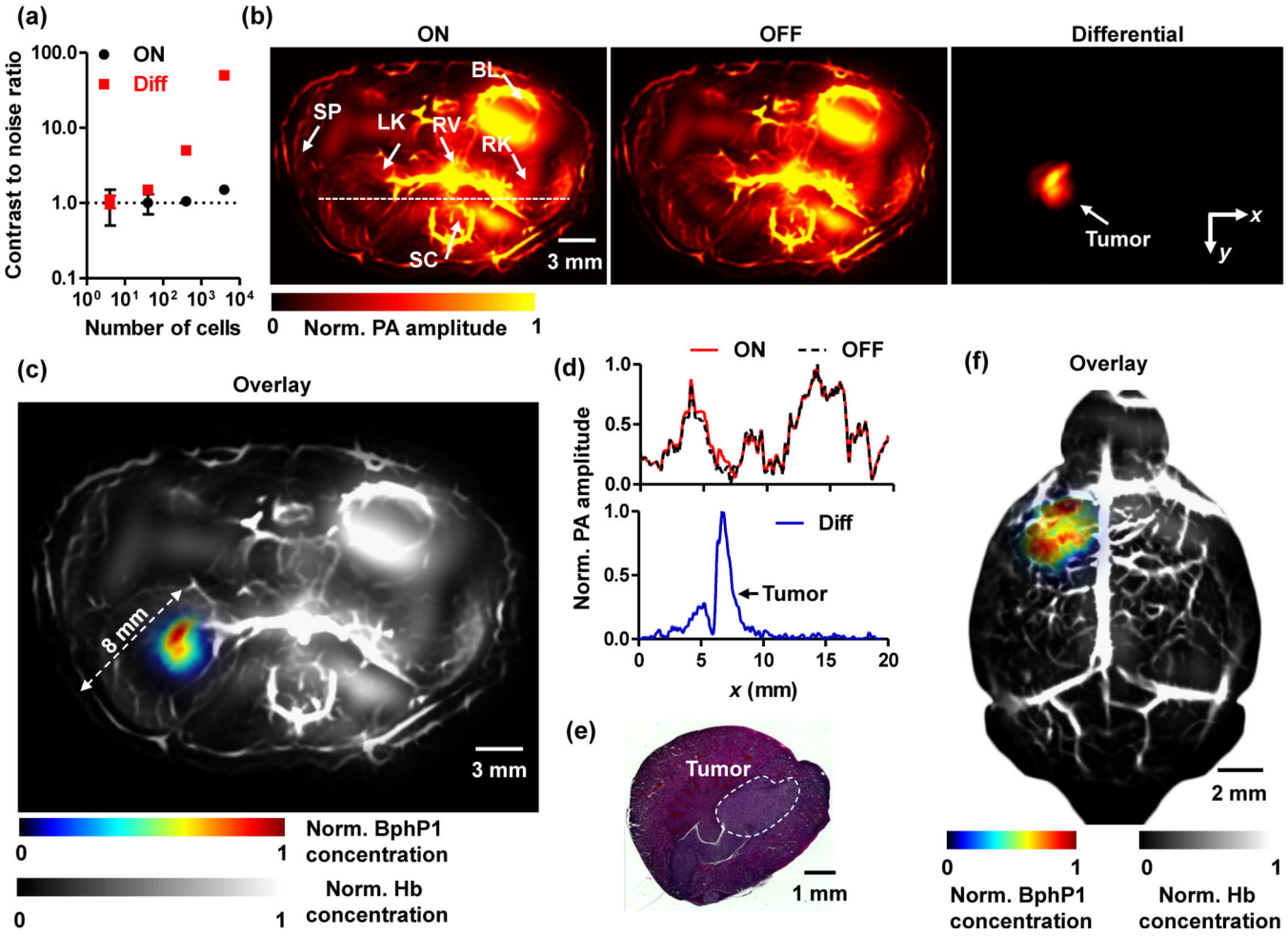

Fig. 3.

Deep PACT of genetically encoded reversibly switchable BphP1 *in vivo*. (a) PA contrast to noise ratio (CNR) of BphP1-expressing U87 cells embedded at 10 mm depth versus increasing cell counts, quantified from ON state and differential PA images shown in Supplementary Fig. 4b. Error bars, s.d. (b) *In vivo* whole-body PACT images of the kidney region of a nude mouse, acquired one week after injection of ~10^6 BphP1-expressing U87 cells into the left kidney. The ON and OFF state PA images clearly show the major blood-enriched internal organs, including the left kidney (LK), right kidney (RK), spinal cord (SC), renal vein (RV), bladder (BL), and spleen (SP). The differential image clearly reveals the tumor in the left kidney. (c) An overlay of the U87 tumor (shown in color) in the left kidney and the blood-dominated OFF state image (shown in gray). (d) Normalized signal profiles of the ON state, OFF state, and differential images along the white dashed line in (b). (e) A representative H&E histological image of the harvested left kidney, showing the tumor region. (f) Deep PACT of a mouse brain U87 tumor expressing BphP1. The tumor (shown in color) was ~3 mm beneath the scalp surface. A global threshold was applied to all the differential images with a threshold level at three times the noise level.

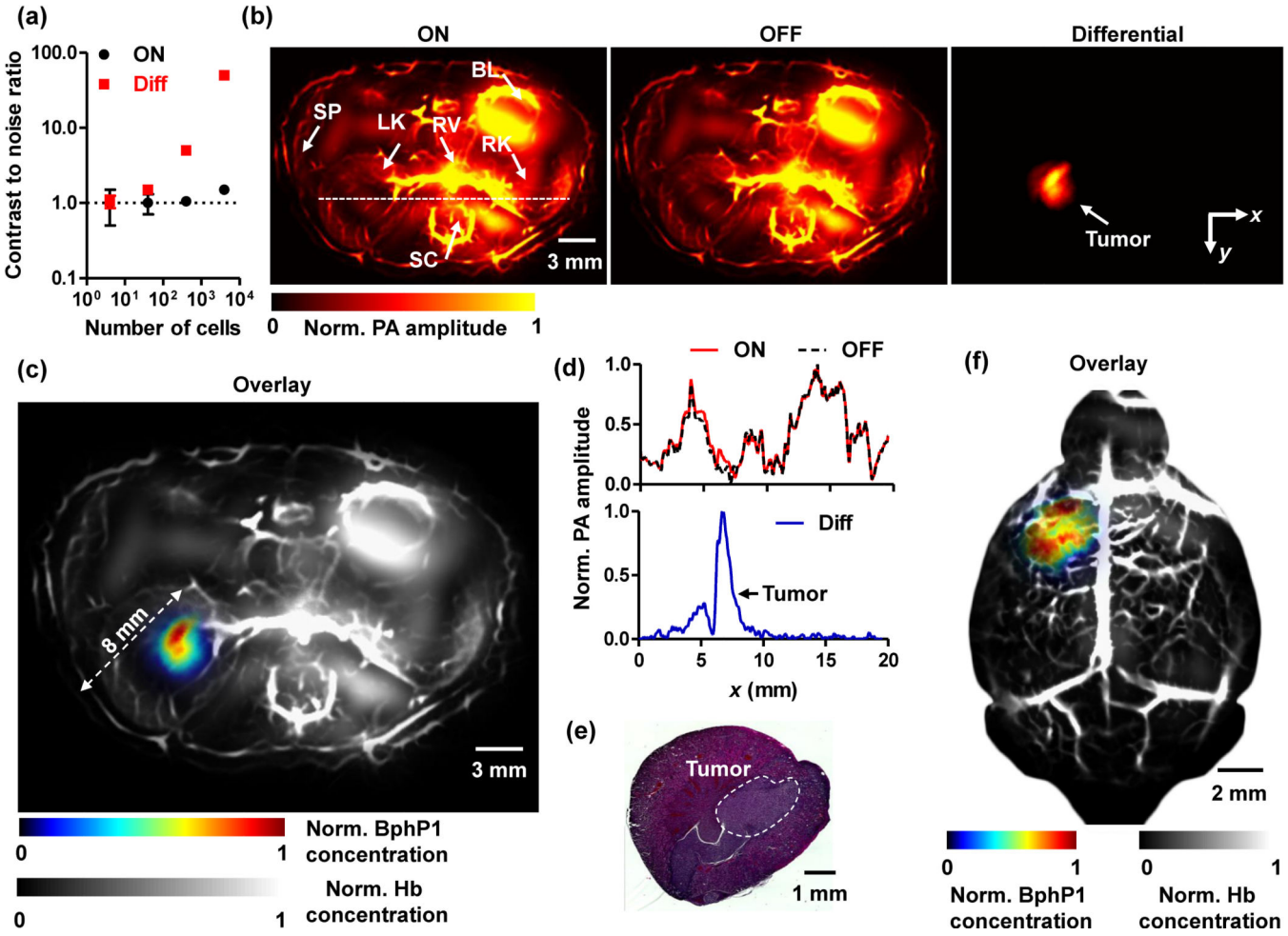

Fig. 4.

Longitudinal PACT monitoring of cancer metastasis in a mouse liver ($n = 6$). (a) Whole-body PACT images of the liver region of a representative nude mouse acquired repeatedly for 30 days after the injection of BphP1-expressing U87 cells into the right liver lobe ($n = 6$). Differential signals (shown in color) are overlaid on top of the structural signals from the blood (shown in gray). The white arrows in the Day 21 and Day 30 images indicate secondary tumors due to metastasis. A global threshold was applied to all the differential images with a threshold level at three times the noise level. All the images were first thresholded and then normalized across the measurements. (b) Increase in areas of the primary and secondary tumors. Error bars: standard errors of the results from 6 animals. (c) Representative H&E histological images of the mouse liver lobes with the primary tumor (PT, top panel) and secondary tumors (ST, bottom panel).

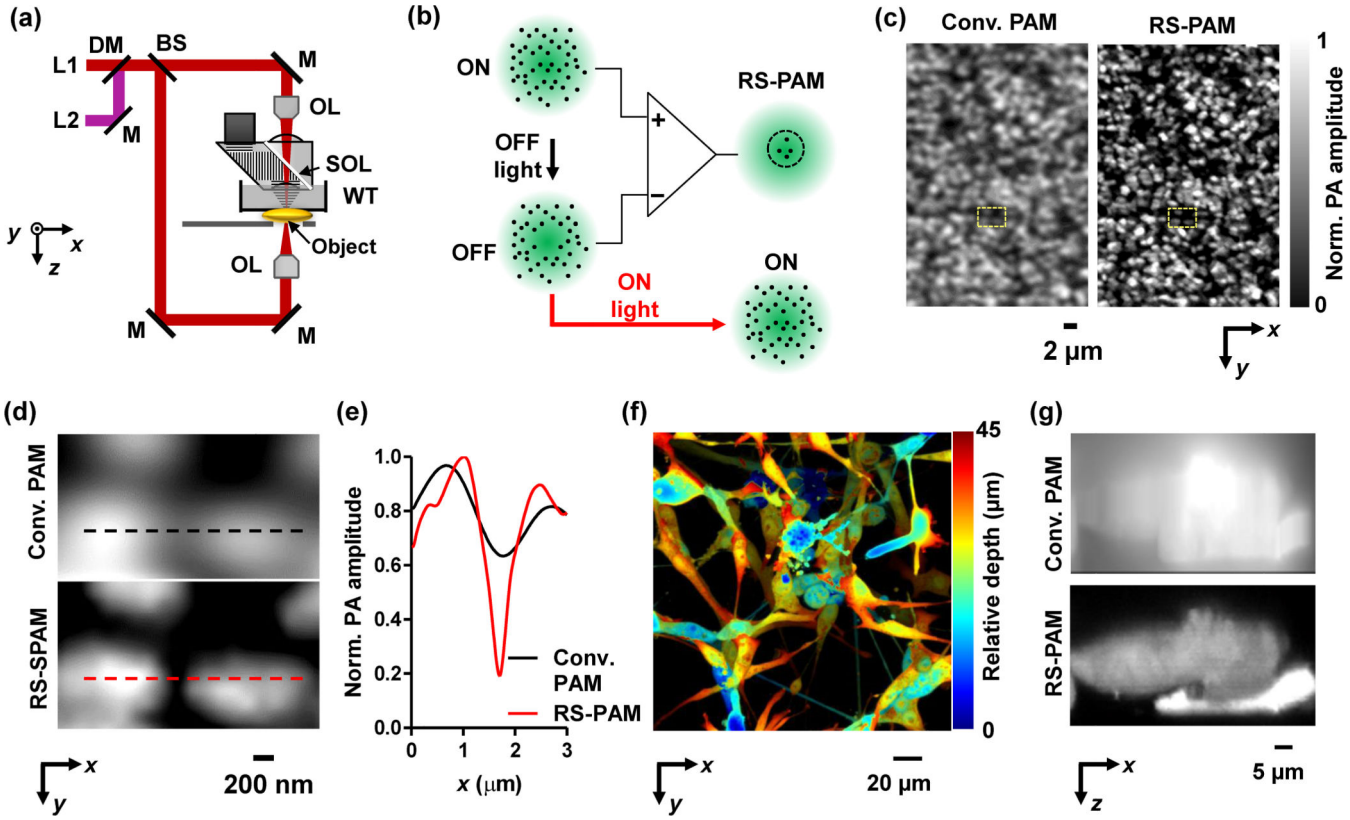

Fig. 5.

Sub-diffraction photoacoustic microscopy of reversibly switchable BphP1 (RS-PAM). (a) Schematic of the double-illumination photoacoustic microscopy system. BS, beam splitter; DM, dichroic mirror; L1–2, laser beam 1 and 2; M, mirror; OL, optical lens; SOL, silicone oil layer; WT, water tank. Top objective NA: 0.1; Bottom objective NA: 1.4 with oil immersion. (b) Principle of RS-PAM with sub-diffraction resolutions. Within the diffraction-limited excitation volume, some ON state BphP1 molecules (red dots) are switched to the OFF state, where the switching-off rate is proportional to the local excitation intensity. By fitting the nonlinear signal decay dynamics, RS-PAM improves the spatial resolution in all dimensions. (c) Conventional PAM and RS-PAM images of BphP1-expressing bacteria densely fixed on a cover glass, showing the superior lateral resolution of RS-PAM. (d) Close-up images of the dashed box regions in (c). (e) Normalized signal profiles across the two bacteria along the dashed lines in (d). (f) Depth-encoded RS-PAM image of a multiple layer of BphP1-expressing U87 cells fixed on a cover glass. The relative depths of the cells are color encoded from blue (superficial) to red (deep). (g) *x*–*z* cross-sectional images of two stacked U87 cells, acquired with conventional PAM and RS-PAM, showing the substantially finer axial resolution of RS-PAM.

Table 1

Optical and photoacoustic properties of the purified BphP1, rsTagRFP and iRFP720.

Protein	Chromophore state	Maximum absorption wavelength, nm	Maximum emission wavelength, nm	Molar extinction coefficient, $M^{-1}cm^{-1}$	Fluorescence quantum yield, %	PA excitation wavelength, nm[a]	PA signal to noise ratio[b]		PA switching ratio[c]		Differential PA image contrast (protein/blood[d]) to noise ratio	
							0 mm depth	10 mm depth	0 mm depth	10 mm depth	0 mm depth	10 mm depth
iRFP720	Pr (ON)	702	720	96,000	6.0	715	610.2 ± 18.4	6.2 ± 0.2	1.0	1.0	None	None
rsTagRFP	ON	567	585	36,800	11.0	567	301.7 ± 10.6	1.2 ± 0.1	8.5 ± 0.3	None	260.2 ± 9.3	None
	OFF	440	585	15,300	0.1							
BphP1	Pfr (ON)	756	None	78,300	None	780	501.4 ± 15.3	15.2 ± 0.3	4.3 ± 0.2	2.8 ± 0.2	380.3 ± 12.0	21.3 ± 0.2
	Pr (OFF)	678	None	87,500	None							

[a] Laser fluence was 8 mJ/cm^2. The wavelengths were chosen based on the absorption of the proteins and the power spectra of the lasers.

[b] Protein concentration was 30 μM, and reduced scattering coefficient of the media was ~10 cm^{-1}.

[c] The switching ratio is the ratio of the PA signal amplitudes acquired in the ON and OFF states.

[d] The hemoglobin concentration was 2.3 mM.